Lawrence Berkeley National Laboratory
LBL Publications

Title
Reliability investigation of the instrument transfer function calibration technique based on binary pseudo-random array standards

Permalink
https://escholarship.org/uc/item/1q1535dc

ISBN
9781510654648

Authors
Yashchuk, Valeriy V
Munechika, Keiko
Rochester, Simon
et al.

Publication Date
2022-10-04

DOI
10.1117/12.2633476

Peer reviewed

eScholarship.org Powered by the California Digital Library
University of California

Reliability investigation of the instrument transfer function calibration technique based on binary pseudo-random array standards

Valeriy V. Yashchuk,[a,*] Keiko Munechika,[b] Simon Rochester,[c] Weilun Chao,[d] Ian Lacey,[a]
Carlos Pina-Hernandez,[b] and Peter Z. Takacs[e]
[a]Advanced Light Source, Lawrence Berkeley National Laboratory, Berkeley, CA 94720, USA;
[b]HighRI Optics, Inc., 5401 Broadway Terr, St. 304, Oakland, CA 94618, USA;
[c]Rochester Scientific, LLC, 2041 Tapscott Ave., El Cerrito, CA 94530, USA;
[d]Materials Sciences Division, Lawrence Berkeley National Laboratory, Berkeley, CA 94720, USA;
[e]Surface Metrology Solutions LLC, 19 S 1st St., Minneapolis, MN 55401 USA

ABSTRACT

The reliability of the instrument transfer function (ITF) calibration technique based on binary pseudo-random array (BPRA) standards is investigated and demonstrated in application to interferometric microscopes. We demonstrate the linearity of the calibration (that is, independence of the ITF calibration on the standards root-mean-square roughness) via comparison of the ITF measurements with a number of artifacts with the etched depth varying from 30 nm to 120 nm. We also show that the calibration does not depend on the surface reflectivity, at least in the range between ~36% and ~80%. The criteria for selection of the geometrical parameters of the BPRA standard design appropriate for a particular interferometric microscope arrangement (including optical magnification), as well as the data acquisition and analysis procedures for different applications are also discussed.

Keywords: calibration, instrument transfer function, binary pseudo-random, test standard, power spectral density, interferometric microscopes, aberration, surface metrology.

1. INTRODUCTON

High accuracy measurements of surface topography of optical elements, especially the ones developed for x-ray applications, require thorough characterization (calibration) of the metrology tool in use and implementation of the results of the calibration in order to understand and, if possible, to suppress the measurement errors due to the tool's performance limitations and imperfections. One of the most challenging tasks of the calibration is the high accuracy measurement of the instrument transfer function (ITF) that describes the tool lateral resolution in the spatial frequency domain (for review, see, for example, Refs. [1-5] and references therein).

Here, we continue to explore the ITF calibration techniques based on test standards structured according to binary pseudo-random (BPR) one-dimensional (1D) sequences (BPR gratings, BPRGs) and two-dimensional (2D) arrays (BPRAs) originally proposed in 2007 [6-8]. From that time, a broad variety of BPR test standards with the elementary sizes from 1.5 nanometers and up to the dozens of microns have been developed and successfully applied for resolution calibration of the electron, x-ray, and optical microscopes, optical scatterometers, and large-aperture Fizeau interferometers (see, for example, Refs. [9-17] and references therein).

A distinguished property of the BPRG and BPRA standards is their inherent power spectral density (PSD) that has a deterministic white-noise-like character. This allows direct determination of the ITF with uniform sensitivity over the entire spatial frequency range and field of view of the instrument under test. As such, the BPRG and BPRA standards satisfy the characteristics of a certifiable ITF calibration artifact: functionality, ease of specification and fabrication, reproducibility, and low sensitivity to manufacturing errors. This is in contrast to most of the common test patterns used in MTF measurements, including knife-edge sources (step-height artifacts) [5,18–22], bar targets [23], sinusoidal [24] and periodical patterns [25,26], which do not meet all these requirements.

*vvyashchuk@lbl.gov; phone 1 510 495-2592; www.lbl.gov.

In the present paper, we discuss our recent investigations of the reliability of the BPRA-standard-based ITF calibration technique in application to optical interferometric microscopes. The paper is organized as follows: In Sec. 2, we briefly describe the interferometric microscope experimental setup, data acquisition and analysis procedures, and the BPRA standards used for the ITF measurements with the microscope. The linearity of the microscope ITF calibration (that is, independence of the calibration on the standards root-mean-square roughness) is demonstrated in Sec. 3 via comparison of the ITF measurements with a number of artifacts with the etched depth varying from 30 nm to 120 nm. In Sec. 4, we show that the calibration does not depend on the surface reflectivity (that could be, for example, due to a nonlinearity of the photon transfer function of the detector's CCD), at least in the range between ~ 36% and ~ 80%. The criteria for selection of the geometrical parameters of the BPRA standard design appropriate for a particular interferometric microscope arrangement (including optical magnification) are discussed in Sec. 5. In conclusion (Sec. 6), we briefly outline our research and development projects in progress and planned with the goal to advance the surface topography metrology of the state-of-the-art x-ray optics via thoroughly accounting for the instrument's calibration.

2. EXPERIMENTAL ARRANGEMENT AND DATA PROCESSING FOR THE OPTICAL INTERFEROMETRIC MICROSCOPE'S ITF CALIBRATION

2.1 Experimental setup

Experimental setup of the interferometric microscope under tests is presented in Fig. 1a as it is located in the Advanced Light Source (ALS) X-Ray Optics Laboratory (XROL) [27,28]. The particle contamination in the XROL cleanroom is routinely better than 200 particles per cubic foot. The room temperature is maintained at 21°C with stability on the level of ± 30 mK. The microscope is mounted on a floating granite table and surrounded with a plastic hutch. This design ensures high stability of the microscope arrangement shown in Fig. 1b. Two BPRA standards, fabricated on 1 in and 2 in diameter super-polished silicon substrates (see Sec. 2.2), are placed on the microscope's two-dimensional translation stage for the measurements. The table in Fig. 1 depicts a set of the microscope magnifications available with different objectives and zoom lenses and the corresponding effective sizes of the microscope's detector pixels.

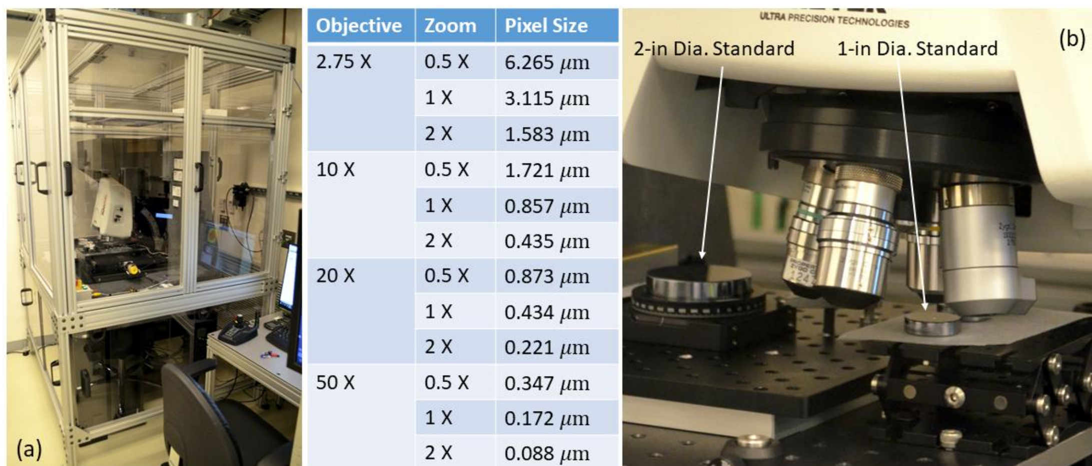

Objective	Zoom	Pixel Size
2.75 X	0.5 X	6.265 μm
	1 X	3.115 μm
	2 X	1.583 μm
10 X	0.5 X	1.721 μm
	1 X	0.857 μm
	2 X	0.435 μm
20 X	0.5 X	0.873 μm
	1 X	0.434 μm
	2 X	0.221 μm
50 X	0.5 X	0.347 μm
	1 X	0.172 μm
	2 X	0.088 μm

Figure 1. (a) Experimental setup of the interferometric microscope and (b) the measurement arrangement of the microscope with the 1-in Dia. BPRA standard; the 2-in Dia. BPRA standard is also seen. The table depicts a set of the microscope magnifications available with different objectives and zoom lenses; the corresponding effective sizes of the microscope's detector pixels are also presented.

2.2 BPRA test samples

For the test measurements discussed in the present paper, we use a number of BPRA standards with different geometrical and optical properties. Figure 2a shows a BPRA standard fabricated on 2-in diameter super-polished silicon substrates by using the nano-fabrication capabilities at the LBNL Molecular Foundry (MF). (The discussion of the fabrication process is out of the scope of this paper; it is described in details, for example, in Refs. [17,29].) The standard has 8 BPRA patterns etched to the substrate. The BPRA patterns A1, B1, C1 and D1 (Fig. 2b) with the smallest fundamental (elementary) sizes of 2.5 µm, 1.2 µm, 800 nm, and 400 nm, respectively (refer to the table of parameters in Fig. 2) are designed according to the prescription for a uniformly redundant array (URA) [30,31]; whereas, the patterns

A2, B2, C2 and D2 with the elementary sizes of 2.501 µm, 1.201 µm, 801 nm, and 401 nm are designed according to the highly randomized (HR) BPR arrays described in Ref. [32]. The step-function pattern E1 that is also etched to the standard is used for cross-comparison investigations in the scope of the analytical modeling of the ITF of the interferometric microscope (see the corresponding discussion in Ref. [33]).

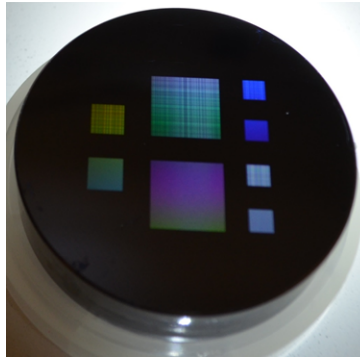

(a)

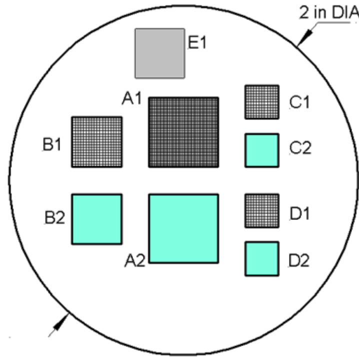

(b)

Uniformly Redundant Array (URA) BPRA Patterns			
	Elementary Size [nm]	Number of Elements, $N_X \times N_Y$	Total Size, X×Y [mm]
A1	2,500	4127×4129	10.32×10.32
B1	1200	4127×4129	4.95×4.95
C1	800	4127×4129	3.30×3.30
D1	400	(2×2)×(4127×4129)	3.30×3.30
Highly Randomized (HR) BPRA Patterns			
A2	2,501	4226×4226	10.57×10.57
B2	1201	4226×4226	5.08×5.08
C2	801	4226×4226	3.39×3.39
D2	401	(2×2)×(4226×4226)	3.39×3.39
Single Step			
	Size [mm]	Number of Elements	Total Size, X×Y [mm]
E1	7.0×7.0	1	7.0×7.0

Figure 2. (a) The 2-in Dia. BPRA standard and (b) the layout of the standard's BPRA patterns. The table depicts the major design parameters of the patterns, the elementary size, number of elements, and the overall area of the BPRA patterns. A step-function pattern E1 is also etched to the standard.

URA-based BPRA patterns generated by sophisticated prescription algorithms [30,31] have PSD distributions that are perfectly constant when evaluated over the entire array. However, the PSDs of the URA-based BPRA pattern subareas, shortened (cropped) and resampled in the course of the ITF measurements, have excess variance [14,32]. Subsequently, the accuracy of the ITF calibration is reduced. Though, as shown in Ref. [14], the 1D PSD noise is significantly lower in measurements with the URA BPRA sample rotated by ~ 45° with respect to the pixel grid of the profiler's detector.

Due to a relatively well-ordered layout of the URA-based BPRA patterns, they, besides the ITF calibration, also facilitate the measurements of the instrument's geometrical distortion. This is exploited in the new version of the data processing software developed for the ITF calibration of metrology profilometers and ITF-based deconvolution of the measured data [33,34].

The HR BPRAs have been specially designed [32] to eliminate the limitation of the URA-based BPRA patterns mentioned above. Consequently, the measurements discussed in this paper are mostly performed over the HR BPRA patterns. In the course of the measurements, we use a number of 2-in Dia. BPRA standards similarly designed, as depicted in Fig. 2, but with different etched depths of about 30 nm, 60 nm, and 120 nm. Additionally, one of the 2-in Dia. BPRA standards with the etched depth of about 30 nm is gold coated in order to significantly increase the surface reflectivity to ~ 80% (at the microscope wavelength of ~ 550 nm) compared to that of the bare silicon of ~ 36%. The comparison of the ITF calibration with the test patterns of different depth and reflectivity allows us to understand the linearity of the microscope's ITF calibration (see Sec. 3) and dependence of the calibration on the test pattern surface reflectivity (see Sec. 4).

As shown in Sec. 5, the 2-in Dia. BPRA standards with the minimum elementary size of the test patterns of 400 nm are good for calibration of the microscope with the objective and zoom lens combination that provides the lateral resolution of about or lower than approximately 800 nm (compare with the microscope's effective pixel size data in Fig.1 table).

In order to calibrate the microscope arranged for higher resolution measurements, we have developed a high resolution BPRA standard fabricated on a 1-in diameter super-polished silicon substrate [17,29] – Fig. 3. The 1-in Dia. standards have three HR BPRA patterns F, G, and H with the elementary sizes of 241 nm, 161 nm, and 81 nm, respectively. The design layout of the 1-in Dia. HR BPRA standard is shown in Fig. 3b. The design parameters of the standard's patterns are presented in Fig. 1 table (see also the corresponding discussion in Ref. [29]).

The 1-in Dia. HR BPRA standard used in this work is uncoated with the etched depth of about 30 nm.

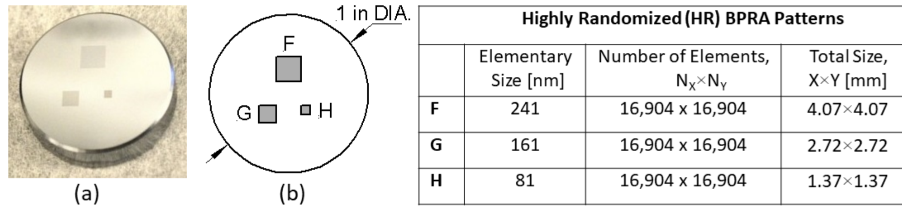

Highly Randomized (HR) BPRA Patterns			
	Elementary Size [nm]	Number of Elements, $N_X \times N_Y$	Total Size, X×Y [mm]
F	241	16,904 x 16,904	4.07×4.07
G	161	16,904 x 16,904	2.72×2.72
H	81	16,904 x 16,904	1.37×1.37

Figure 3. (a) The 1-in Dia. HR BPRA standard and (b) the design layout of the standard's test patterns. The table depicts the major design parameters of the patterns, the elementary size, number of elements, and the overall area of the BPRA patterns.

2.3 Data acquisition and analysis procedures

For the measurements discussed in this paper, the data acquisition and preliminary data processing is performed with the microscope's software. The preprocessing includes subtraction of the reference topography, measured and averaged over a number of unpatterned areas of the standard, and detrending of the best fit plane surface. No filtering is applied.

Next, the preprocessed BPRA pattern height distribution is processed with custom software developed for the ITF calibration of metrology profilometers and ITF-based deconvolution of the measured data [17,34,35]. Figure 4 presents the software screenshot corresponding to the comparison of two measurements over the 1-in Dia. HR BPRA patterns F and H (the elementary sizes of 241 nm and 81 nm, Fig. 3) performed with the interferometric microscope equipped with the 50× objective and 2× zoom lens. In this case, the F-pattern topography data are loaded as the 'Measured' one (the top-left 2D image in the screenshot in Fig. 4), while the H-pattern data is the 'Reference' (the top-right image). The corresponding 1D PSD distributions in the vertical and horizontal directions are shown in the bottom right plots of the screenshot (Fig. 4) with the blue and green curves for the 'Measured' and 'Reference' data, respectively.

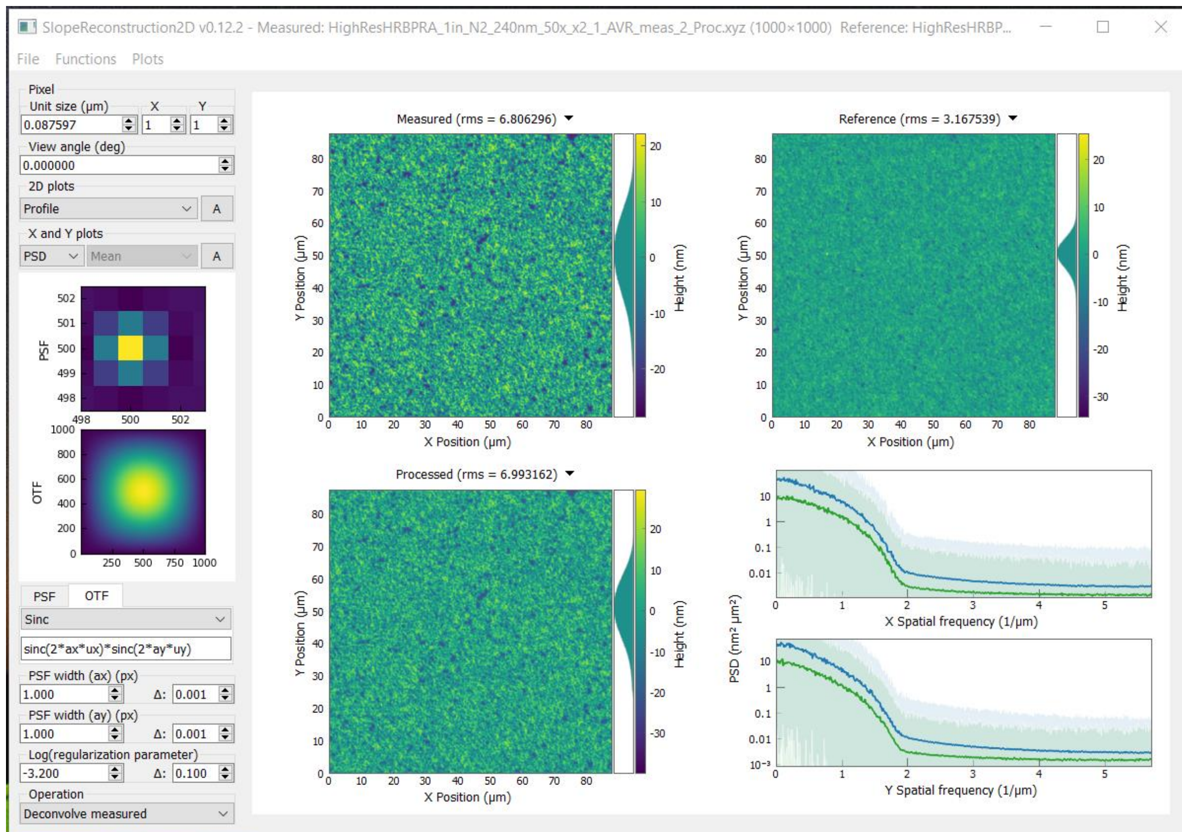

Figure 4. (a) A screenshot of the original software developed for the ITF calibration of metrology profilometers and ITF-based deconvolution of the measured data. A beta-version of a most recent version of the software is presented in Ref. [35]. The data shown has been obtained with the interferometric microscope equipped with the 50× objective and 2× zoom lens.

The software depicted in Fig. 4 is capable for the deconvolution of the measured data based on the measured and, then, analytically modeled ITF of the tool in use. In the present work that is mainly devoted to the experimental investigation of repeatability of the ITF calibration results obtained with different HR BPRA standards, we don't actively use the deconvolution capabilities of the software (though, the power of the deconvolution is illustrated in Sec. 6). Nevertheless, the screenshot in Fig. 4 depicts the deconvolution settings corresponding just to a simplest single-pixel sinc-function like ITF model. Obviously, this model does not describe the real ITF of the microscope equipped with the 50× objective and 2× zoom lens. The ITF models more suitable for this case are discussed and treated, for example, in Ref. [33].

3. LINEARITY OF THE MICROSCOPE'S ITF CALIBRATION

For experimental investigation of the linearity of the ITF calibration, we compare the PSD distributions of the equivalent HR BPRA patterns (with the same elementary size) but with different etched depth, about 30 nm, 60 nm, and 120 nm when they are measured at the same microscope arrangement.

The empirical result of the comparison is that with the all available arrangements of the microscope (see Fig. 1 table), the PSD distributions measured with the same microscope arrangement over the equivalent patterns (that is any one of the patterns A2, B2, C2, or D2; refer to Fig. 2) of the 2-in BPRA standards with the different etched depths have a totally identical shape and are different only by a linear scaling factor accounting for the difference of the etched depths.

Figure 5 illustrate this result with an example of the measurements with the microscope equipped with 2.75× objective (1× zoom) over the A2 patterns of the BPRA standards with 30-nm and 60 nm depth. The 1D PSD distributions are identical upon scaling with a factor of 0.49 applied to the height distribution of the 60-nm pattern in order to match the root-mean-square (rms) variations (the surface roughness) of the recorded topographies.

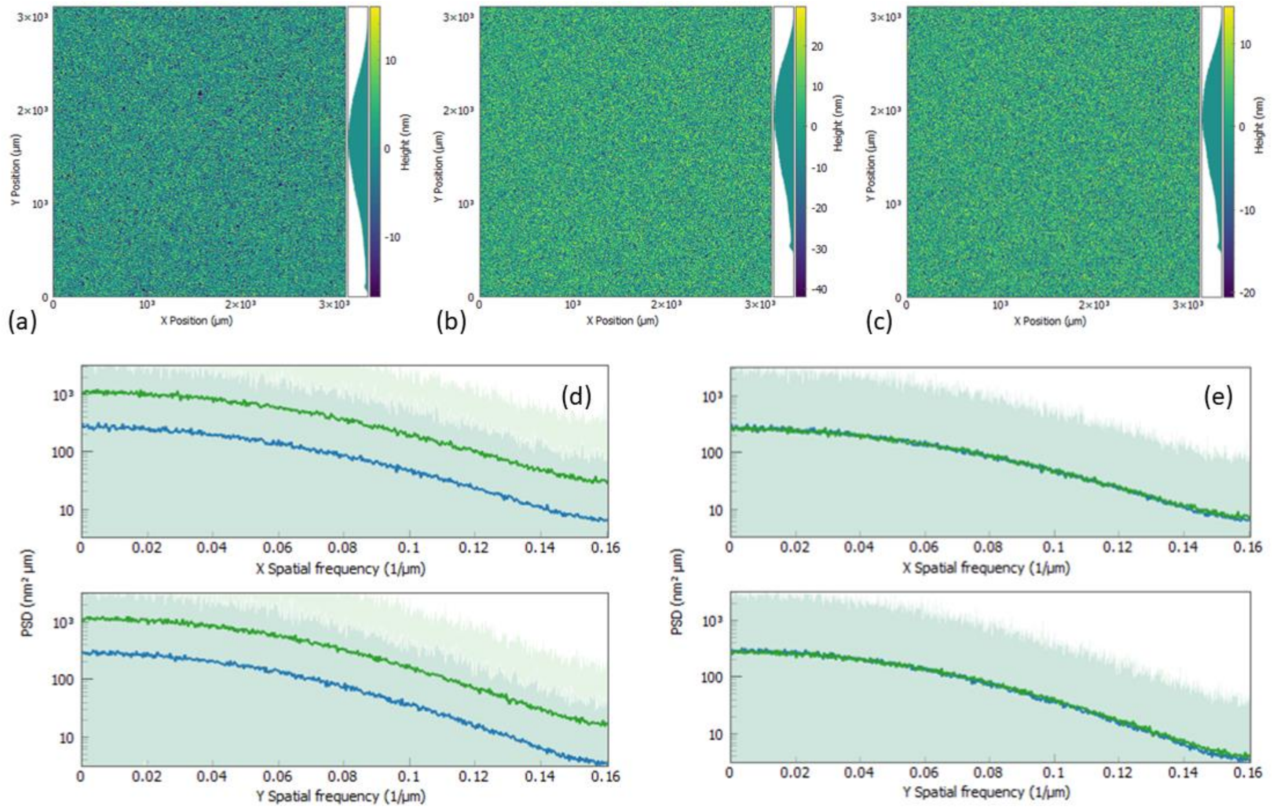

Figure 5. The height topographies of the A2 HR BPRA patterns with (a) 30-nm and (b) 60-nm etched depths, as measured with the interferometric microscope equipped with the 2.75× objective (1× zoom). A single measurement consists of 64 acquisitions; the reference surface is subtracted and the best fit plane surface is subtracted. The surface roughness of the topographies in plots (a) and (b) is 5.97 nm 12.18 nm, respectively. (c) The same height topography as in plot (b) but scaled with a factor of 0.49. (d) The 1D PSD distributions of the original measurements over the patterns with 30 nm (the blue lines) and 60 nm (the green lines) depths. (e) The same PSD distributions as in plot (d) but with the scaling applied.

Figure 6 provides a comparison of the PSD distributions the measurements over the D2 patterns of the BPRA standards with 30-nm and 120 nm depth using the microscope in the same arrangement as in Fig. 5. The PSD spectra are identical upon scaling with a factor of 0.197 applied to the height distribution of the 120-nm pattern in order to match the root-mean-square (rms) variations of the topographies under comparison.

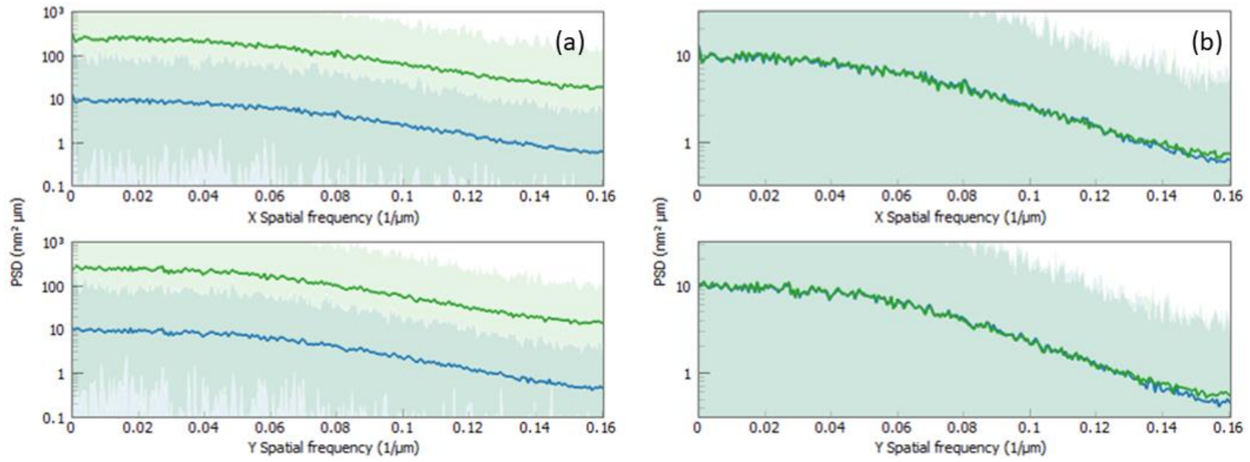

Figure 6. (a) The 1D PSD distributions of the D2 HR BPRA patterns with the 30-nm (the blue lines) and 120-nm (the green lines) depths, as measured with the interferometric microscope equipped with the 2.75× objective (1× zoom). The corresponding rms roughness of the measured height distributions is about 1.2 nm and 6.1 nm, respectively. (b) The same PSD distributions as in plot (a) but after scaling of the measured 30-nm depth height topography with a factor of 0.197. A single measurement consists of 64 acquisitions; the reference surface is subtracted and the best fit plane surface is subtracted. The logarithmically small difference at the highest spatial frequencies is, probably, due to the difference of the random noise of the measurements.

Note that the roughness of the A2 and D2 topographies with the depth of ~ 30 nm observed in the measurements with the same microscope arrangement are significantly different, 5.97 nm and 1.2 nm. This is because of the difference between the elementary sizes (2,501 nm and 401 nm) of the corresponding HR BPRA patterns (A2 and D2) – see Fig. 2. Due to the limited resolution of the microscope with the effective pixel size of about 3.1 µm, the high spatial variations of the 401-nm D2 pattern are affectively averaged upon the measurements.

4. INDEPENDENCE OF THE MICROSCOPE'S ITF CALIBRATION ON THE SURFACE REFLECTIVITY OF THE BPRA TEST STANDARD

The surface reflectivity dependence (that could be, for example, due to a nonlinearity of the photon transfer function of the detector's CCD) of the ITF calibration based on the BPRA technique has been tested with the interferometric microscope available at the ALS XROL by comparing the measured PSD distributions of the equivalent HR BPRA patterns (with the same elementary size) of the uncoated (bare silicone) and gold-coated 2-in BPRA standards when they are measured with the microscope at the same arrangement.

A typical result of the tests is depicted in Fig. 7 that shows in plot (a) the 1D PSD distributions of the uncoated and gold-coated B2 patterns (with the elementary size of 1,201 nm) measured with the microscope equipped with 2.75× objective (1× zoom). Each measurement consists of 64 acquisitions. Before the PSD calculation, the reference surface is subtracted and the best fit plane surface is detrended from the raw measured topography. In spite of the mutual shift of the PSDs in Fig. 7a, their shapes are really identical. This can be seen in plot (b), where the PSD corresponding to the surface height topography of the uncoated B2 BPRA pattern [the green line in plot (a)] is recalculated for the height distribution scaled down by a factor of 0.833.

Similarly, the comparison of the PSDs of the equivalent BPRA patterns of the uncoated and coated 2-in BPRA standards measured with all available arrangements of the microscope confirms the identity of the PSD shapes. The difference of the PSDs accounted for by a linear scaling factor, is due to the slightly different etched depths of the two standards. Therefore, we conclude that the ITF measured with the same microscope arrangement over the equivalent patterns does not depend on the surface reflectivity of the test standard at least in the reflectivity range between ~ 36% (the bare silicone) and ~80% (the gold coating).

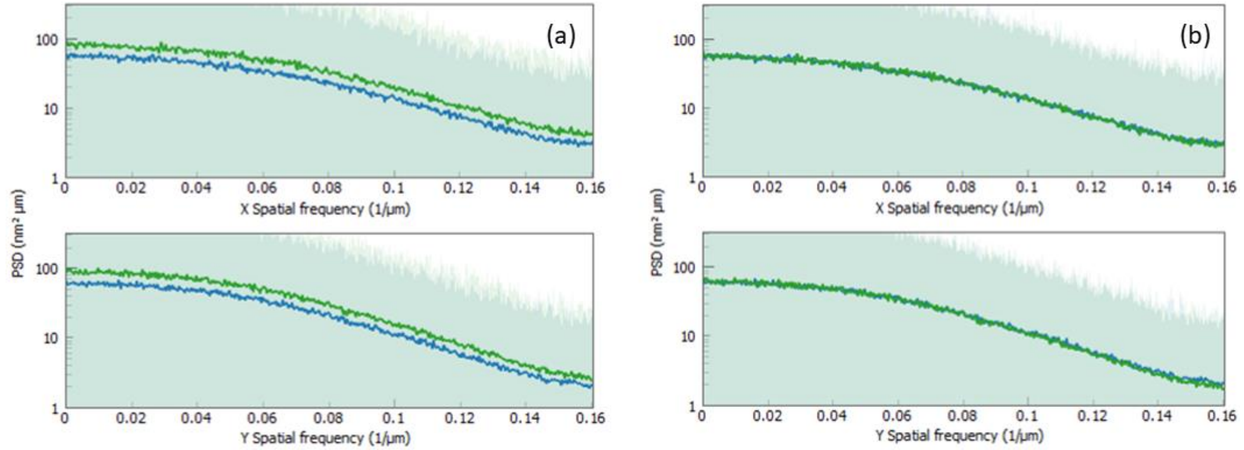

Figure 7. (a) The 1D PSD distributions of the uncoated (the green line) and gold-coated (the blue line) B2 patterns measured with the microscope equipped with 2.75× objective (1× zoom). The corresponding rms roughness of the measured height distributions is about 3.51 nm and 2.92 nm, respectively. (b) The same PSD distributions as in plot (a) but after scaling of the measured uncoated height topography with a factor of 0.833. A single measurement consists of 64 acquisitions; the reference surface is subtracted and the best fit plane surface is detrended. The scaling accounts for the slightly different etched depths of the two standards used for the tests.

5. SELECTION OF AN APPROPRIATE BPRA STANDARD

5.1 URA BPRA standards vs HR BPRA standards

In the Secs. 3 and 4, we have experimentally proven that the results of the ITF calibration of the ALS XROL interferometric microscope are practically identical when the HR BPRA with the same design (with the same elementary size), but with different etched depth and surface reflectivity are used for the calibration. This is also true for the ITF measurements with the URA-based BPRA patterns.

Selection between URA and HR BPRA design depends on the scope of the tests desired. As mentioned above, due to the relatively well-ordered layout of the URA-based BPRA patterns, they can be useful for measuring the instrument's geometrical distortion [35]. In this case, the excess noise of the ITF measurements with the URA BPRA patterns can be effectively suppressed by rotation of the pattern by ~ 45 degrees with respect to the instrument's pixel grid [14].

When ultimate accuracy of the 2D ITF calibration is required, the HR BPRA patterns are preferable ensuring a lower noise and independence on the pattern alignment. This can be understood by comparing the height distributions and 1D PSDs measured with the D2 HR BPRA pattern (with the elementary size of 401 nm; the etched depth of 60 nm) oriented almost parallel and rotated by approximately 45 degrees with respect to the instrument's detector pixel grid – Fig. 8.

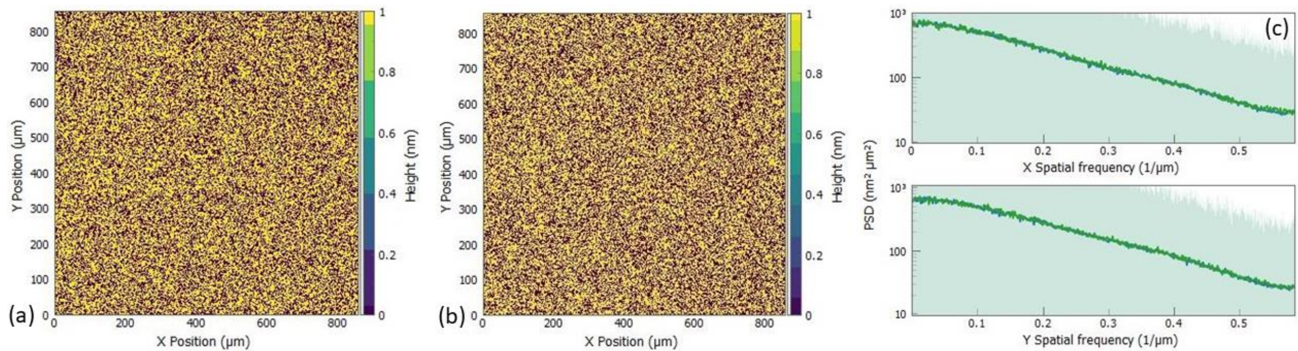

Figure 8. The surface height topographies of the D2 BPRA pattern measured with the microscope equipped with 10× objective (1× zoom) in almost parallel (a) and (b) rotated by ~ 45 degree orientations with respect to the microscope's pixel grid. The corresponding rms roughness of the measured height distributions are the same, ~ 16.8 nm. (c) The 1D PSD distributions of the unrotated (the blue line) and rotated (the green line) D2 pattern. A single measurement consists of 1 acquisition; the reference surface is subtracted and the best fit plane surface is detrended.

In the case depicted in Fig. 8, the microscope is equipped with the 10× objective at 1× zoom; the effective pixel size is 857 nm (see Fig. 1 table). The PSD distributions of the unrotated and rotated patterns perfectly coincide (Fig. 8c) that is principally different from the case of the URA BPRA patterns [14].

5.2 Selection of the pattern elementary size

The most challenging question when selecting an appropriate BPRA standard pattern for characterization of an interferometric microscope is the pattern elementary size.

If the URA BPRA pattern is used for the characterization of the microscope's geometrical distortion, the elementary size of the pattern should be large enough to be well resolved in the measurements. We have empirically determined that the geometrical distortion calibration can be efficiently performed with the URA BPRA pattern with elementary size larger than the microscope lateral resolution by a factor of 2-3 (for more details, see corresponding discussion in Ref. [35]).

In order to provide a reliable ITF calibration, the elementary size of the BPRA test pattern has to be significantly smaller than the instrument lateral resolution. The microscope lateral resolution is mostly limited by the effective pixel size down to the microscope's resolution limit comparable to the probe light wavelength (in our case, this is about 550 nm). This is the case, for example, of the measurements with the 2.75× at 1× zoom, presented in Figs. 5-7.

At the high magnification arrangements, as the one depicted, for example, in Fig. 4, the effective pixel size of the microscope equipped with the 50× objective and 2× zoom lens is about 88 nm. This is significantly smaller than the microscope's resolution limit of ~ 500 nm (the Abbe diffraction limit at the objective NA=0.55). In such case, the microscope lateral resolution is mostly limited by the microscope optical system, rather than the detector effective pixel size – see Fig. 4. The relatively small effective pixel size determines the correspondingly large spatial frequency range of the PSD distributions calculated from the 'oversampled' measurements. Therefore, the question is if one should use the BPRA pattern with the spatial frequency range comparable with, or even larger than that of the microscope. The measurements in Fig. 4 can be considered as an empirical answer to this question. For our microscope equipped with the 50× objective and 2× zoom lens, the measured PSD distributions have absolutely the same shape for the 241-nm and 81-nm HR BPRA patterns. Therefore, the results of the ITF calibration in these measurement are identical.

The microscope arrangement with the 10× objective at 1× zoom (effective pixel size of ~550 nm) used for measurements with D2 pattern of the HR BPRA (Fig. 8) represents an in-between case where the lateral resolution is significantly affected by both, the effective pixel size and the optical system of the microscope. For more detailed discussion, see, for example, Refs. [4,5,33] and references therein. Here, we just provide the reader with empirical data that can be useful for practical application of the ITF calibration technique based on the BPRA test standards. Figure 9 presents the results of the ITF measurements of the ALS XROL interferometric microscope equipped with the 10× objective at 1× zoom. The 241-nm F and 81-nm H patterns of the high resolution 1-in HR BPRA standard (Fig. 3) are used.

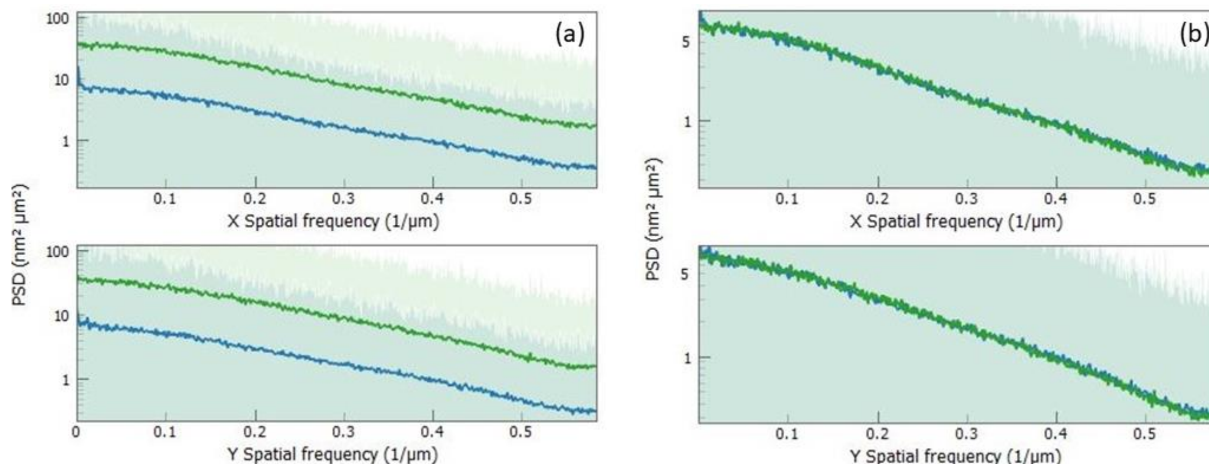

Figure 9. (a) The 1D PSD distributions of the F (the green line) and H patterns (the blue line) of the high resolution 1-in HR BPRA standard (with 241-nm and 81-nm elementary sizes) measured with the microscope equipped with the 10× objective (1× zoom). The corresponding rms roughness of the measured height distributions is about 3.94 nm and 1.75 nm. (b) The same PSD distributions as in plot (a) but after scaling of the measured F-pattern topography with a factor of 0.444. A single measurement consists of 1 acquisition; the reference surface is subtracted and the best fit plane surface is detrended.

A remarkable result from the measurements presented in Fig. 9 is that in spite of the significant, a factor of 3, difference of the inherent spatial frequencies of the F and H patterns, the measured PSD distributions have exactly the same shape. The scaling applied to completely match the PSDs (Fig. 9b) accounts for the difference between the spatial frequency ranges of the patterns. The higher spatial frequency variations of the H-pattern are more effectively averaged out due to the limited lateral resolution of the microscope.

To conclude this section, in Fig. 10, we compare the measurement with 81-nm HR BPRA pattern, depicted in Fig. 9, with the one performed with the unrotated 401-nm D2 HR BPRA pattern, displayed in Fig. 8.

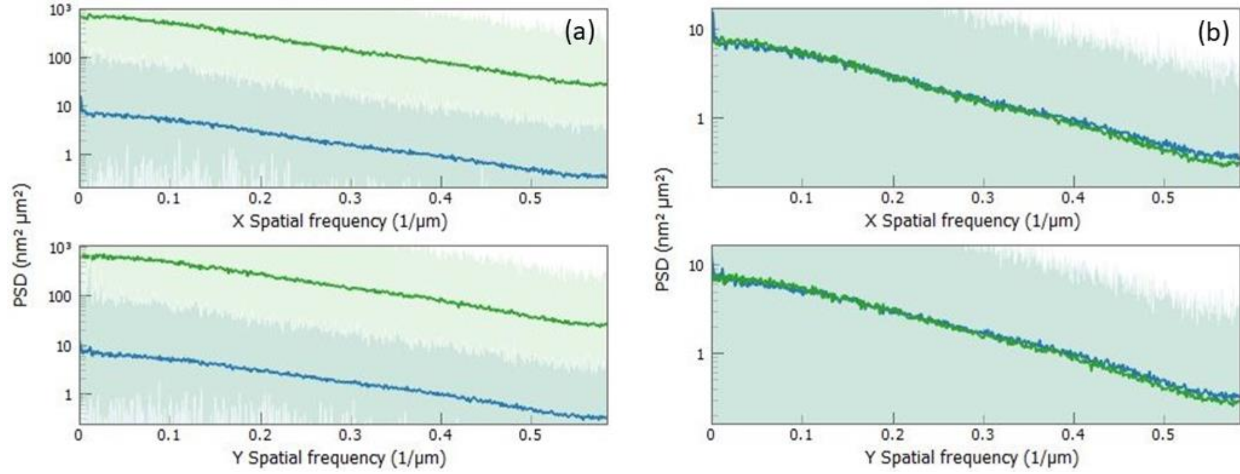

Figure 10. (a) The 1D PSD distributions of the D2 (the green line) and H (the blue line) patterns with the elementary sizes of 401 nm and 81 nm as measured with the microscope equipped with the 10× objective (1× zoom). The corresponding rms roughness of the measured height distributions is about 16.79 nm and 1.75 nm, respectively. (b) The same PSD distributions as in plot (a) but after scaling of the measured D2-pattern topography with a factor of 0.1042. A single measurement consists of 1 acquisition; the reference surface is subtracted and the best fit plane surface is detrended.

Almost over the entire spatial frequency range of the microscope, the PSD distributions obtained with the HR BPRA patterns with the elementary sizes different by a factor of 5 have the same shape. The observed difference of the PSDs at the higher spatial frequencies are probably due to the significantly different contributions of the resampling effect (see Ref. [33] and discussion in Sec. 6, below). In any case the difference is very small, so that the associated error of the ITF calibration with the D2-pattern is less than 0.01 compared with the ITF close to one at the lowest spatial frequencies.

Note that the almost perfect matching of the PSDs measured with the 81-nm and 241-nm patterns (Fig. 9) suggests that the resampling effect is almost negligible in the case of the 241-nm patterns. Therefore, we can conclude that for a reliable ITF calibration of the microscope, we should select the HR BPRA patterns that have the elementary sizes smaller than the microscope lateral resolution by a factor of ≥ 3. However, even if the factor is just about 2, the calibration error is rather low. Moreover, a straightforward accounting for the resampling effect allows to completely overcome the problem [33].

6. DISCUSSION AND CONCLUSIONS

We have presented the results of the experimental (empirical) investigation of the reliability of the instrument transfer function calibration technique based on binary pseudo-random array standards when the technique is applied to the ALS XROL interferometric microscope intended for high precision surface topography measurements with x-ray optics.

We have experimentally proven that the ITF calibration of the microscope is practically independent on the etched depth (at least, over the examined depth range of ~ 30 nm – 120 nm) and on the surface reflectivity (at least, in the reflectivity range between ~ 36% and 80%) of the BPRA pattern used for the calibration. This conclusion is valid for the ITF measurements with the BPRA patterns designed based on both, the URA and HR prescriptions.

For the BPRA standard based ITF calibration, we exploit the inherent (upon design and fabrication) property of the standards' test patterns to possess while-noise-like surface topography described with the power spectral density independent of the spatial frequencies over the entire dynamic range of the BPRA pattern in use. Indeed, the inherent

PSD of a particular BPRA pattern as designed and fabricated is perfectly constant being evaluated applying the discrete Fourier transform methods to the BPR array with the pixilation determined by the elementary size of the pattern (see, for example, Refs. [7,8,32,33] and references therein).

However, when the BPRA standard is used for calibration of an instrument with effective pixel size significantly different (generally, larger) than the test pattern elementary size, the inherent (for this particular measurement) PSD of the pattern has to be evaluated over the pixel array of the measured topography with the pixilation corresponding to the instrument's effective pixel size. The resultant measurement-specific inherent PSD of the test pattern is affected by the resampling from the pattern array pixilation to that of the measurement. It is straightforward to show [33,36], that the resampling effect is specific to the test pattern array and the measurement array grid, rather than to depend on the height value distribution over the pattern pixels. Thus, in the PSD domain, the resampling effect is the same for the binary and for the real random variations of the height values.

It can be also shown [36] that the resampling effect to 1D PSDs of a BPRA pattern can be modeled with a multiplication function in the form of $a+b\cos\left(2\pi k/N\right)$, where a and b are the constants, and the spatial frequency parameter k varies from 0 up to $N/2$, corresponding to the Nyquist frequency of the measured topography with total number of pixels of N in the direction of the 1D PSD. The values of the constants a and b are determined by the specific values of the pixilation and size (number of pixels) of the test pattern and the measured topography.

In this paper, we have empirically shown that, when using the constant inherent PSD of the test pattern, a reliable (high accuracy) ITF calibration of the microscope is possible with the HR BPRA patterns that have the elementary sizes smaller than the microscope lateral resolution limit (evaluated, for example, as the Abbe diffraction limit) by a factor of $\geq$ 3. However, even if the factor is about 2, the calibration error related to the resampling effect is still rather low. As pointed out above, a straightforward accounting for the resampling effect allows to completely overcome the problem.

We should also note an interesting observation related to the PSD measurements in Fig. 9. In spite of the significantly different (by a factor of 3) inherent spatial frequency ranges of the HR BPRA patterns with the elementary sizes of 81 nm and 241 nm, there is no mark of the aliasing effect (see, for example, Ref. [1]). This is, probably, a signature of an advanced (aliasing-free) design of the microscope. Further investigation of the aliasing effects in measurements with the BPRA standards are in progress (see also discussions in Refs. [33,36]).

For the completeness of the discussion of the BPRA-based ITF calibration technique, Fig. 11 depict an example of the microscope data deconvolution based on the ITF calibration. In this case, the surface height topography of a 401-nm HR BPRA pattern is measured with the microscope equipped with 2.75× objective (1× zoom) – Fig. 11a. At the microscope arrangement with such low resolution (with the effective pixel size of about 3.1 μm – see Fig. 1 table), the ITF is expected to be reasonably well modeled with the one-pixel sinc-function. The result of the deconvolution with the sinc-function like ITF is depicted in Fig. 11b.

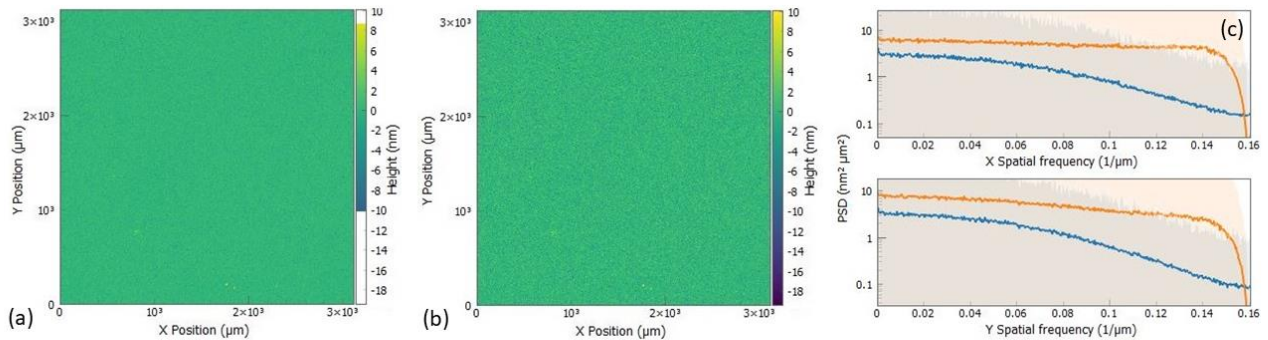

Figure 11. (a) The surface height topographies of the 401-nm HR BPRA pattern as measured with the microscope equipped with 2.75× objective (1× zoom) and (b) the result of the deconvolution with the sinc-function like one-pixel ITF of the height distribution in plot (a). The corresponding rms roughness of the measured and deconvolved height distributions is ~ 0.67 nm and ~ 1.22 nm, respectively. (c) The 1D PSD distributions of the measured (blue line) and deconvolved (orange line) BPRA topographies. A single measurement consists of 64 acquisitions; the reference surface is subtracted and the best fit plane surface is detrended.

In spite of the visually undistinguished measured and deconvolved topographies, the roughness is different by a factor of approximately 2, being ~ 0.67 nm and ~ 1.22 nm, respectively. This can be thought of as an illustration of how the application of metrology data deconvolution based on the experimentally measured ITF, can advance the confidence of surface topography metrology with state-of-the-art x-ray optics. Note that this point has been experimentally justified in application to surface slope metrology with super high quality x-ray optics [37,38].

The effect of the deconvolution is clearly seen in the corresponding 1D PSD – Fig.11c. The 1D PSD distribution of the deconvolved 401 nm HR BPRA topography (the orange line in Fig. 11c) is significantly more flat, depicting the inherent constant PSD of the test pattern. However, there is a noticeable deviation from the expected constant PSD level, especially in the bottom PSD plot corresponding to the left-to-right direction of the measured topography. Because of the extreme difference between the pattern elementary size and the microscope lateral resolution (by almost a factor of 8), the deviation of the deconvolved 1D PSDs from a constant shape cannot be explained by the resampling effect. Really, the deconvolved PSD distributions indicate a significant temporal instability of the measurement with 64 acquisitions averaged for each measurements. Due to the mechanical design of the microscope, the instability in two directions are different evidenced by the different shape of the corresponding 1D PSD distributions.

The deconvolution data presented in Fig. 11 can serve as an illustration of the power and usefulness of the BPRA-based ITF calibration technique discussed throughout the present paper with the examples of multiple measurements with the ALS XROL interferometric microscope in very different arrangements. However, this is still a single microscope that generally can be different from other optical microscope available for surface metrology. Therefore, application of the developed calibration and performance characterization techniques to similar instruments is very interesting and important. Partially, this task is partially accomplished in Ref. [39] and in a paper at this conference [40].

ACKNOWLEDGEMENTS

The authors are grateful to Alexander Givental, Ulf Griesmann, and Alan Roginsky for fruitful discussions. This work was partially supported by the U.S. Department of Energy Office of Science, Office of Basic Energy Sciences, and Small Business Technology Transfer (STTR) programs under Award Numbers DE-SC0011352, DE-SC0022373, and DE-SC0022412 to HighRI Optics, Inc. and Rochester Scientific, LLC. It was also supported by the U.S. NASA STTR programs under Contracts #80NSSC20C0505 and #80NSSC22PB039 to HighRI Optics, Inc. Research at the Advanced Light Source and the Molecular Foundry at Lawrence Berkeley National Laboratory are supported by the Office of Science, Office of Basic Energy Sciences, and Material Science Division of the U.S. Department of Energy under Contract No. DE-AC02-05CH11231.

DISCLAIMER

This document was prepared as an account of work sponsored by the United States Government. While this document is believed to contain correct information, neither the United States Government nor any agency thereof, nor The Regents of the University of California, nor any of their employees, makes any warranty, express or implied, or assumes any legal responsibility for the accuracy, completeness, or usefulness of any information, apparatus, product, or process disclosed, or represents that its use would not infringe privately owned rights. Reference herein to any specific commercial product, process, or service by its trade name, trademark, manufacturer, or otherwise, does not necessarily constitute or imply its endorsement, recommendation, or favor by the United States Government or any agency thereof, or The Regents of the University of California. The views and opinions of authors expressed herein do not necessarily state or reflect those of the United States Government or any agency thereof or The Regents of the University of California.

REFERENCES

[1] Boreman, G. D., [Modulation Transfer Function in Optical and Electro-optical Systems], SPIE Press, Bellingham, Washington (2001).

[2] ISO, 25178-600: Geometrical Product Specification (GPS) – Surface Texture: Areal – Part 600: Metrological Characteristics for Areal-topography Measuring Methods (International Organization for Standardization, 2019); https://www.iso.org/standard/67651.html.

[3] de Villiers, G. and Pike, E. R., [The Limits of Resolution], CRC Press, London & New York (2019).
[4] Foreman, M. R., Giusca, C. L., Coupland, J. M., Torok, P., Leach, R. K., "Determination of the transfer function for optical surface topography measuring instruments - a review," Meas. Sci. Technol. 24, 052001/1-18 (2013); doi:10.1088/0957-0233/24/5/052001.
[5] de Groot, P. J., "The instrument transfer function for optical measurements of surface topography," J. Phys. Photonics 3, 024004/1-16 (2021); doi: https://doi.org/10.1088/2515-7647/abe3da.
[6] Yashchuk, V. V., McKinney, W. R., and Takacs, P. Z., "Test surfaces useful for calibration of surface profilometers," United States Patent No.: 8,616,044.
[7] Yashchuk, V. V., McKinney, W. R., and Takacs, P. Z., "Binary pseudorandom grating as a standard test surface for measurement of modulation transfer function of interferometric microscopes, Proc. SPIE 6704, 670408 (2007); https://doi.org/10.1117/12.732557.
[8] Yashchuk, V. V., McKinney, W. R., and Takacs, P. Z., "Binary pseudorandom grating standard for calibration of surface profilometers," Opt. Eng. 47(7), 073602-1-5 (2008); https://doi.org/10.1117/1.2955798.
[9] Barber, S. K., Anderson, E. D., Cambie, R., McKinney, W. R., Takacs, P. Z., Stover, J. C., Voronov, D. L., and Yashchuk, V. V., "Binary pseudo-random gratings and arrays for calibration of modulation transfer function of surface profilometers," Nucl. Instr. and Meth. A 616, 172-182 (2010); https://doi.org/10.1016/j.nima.2009.11.046.
[10] Yashchuk, V. V., Conley, R., Anderson, E. H., Barber, S. K., Bouet, N., McKinney, W. R., Takacs, P. Z., and Voronov, D. L., "Characterization of electron microscopes with binary pseudo-random multilayer test samples," Nucl. Instr. and Meth. A 649(1), 150-152 (2011); doi: 10.1016/j.nima.2010.11.124.
[11] Yashchuk, V. V., Anderson, E. H., Barber, S. K., Bouet, N., Cambie, R., Conley, R., McKinney, W. R., Takacs, P. Z., Voronov, D. L., "Calibration of the modulation transfer function of surface profilometers with binary pseudo-random test standards: expanding the application range to Fizeau interferometers and electron microscopes," Opt. Eng. 50(9), 093604 (2011); doi: 10.1117/1.3622485.
[12] Yashchuk, V. V., Fischer, P. J., Chan, E. R., Conley, R., McKinney, W. R., Artemiev, N. A., Bouet, N., Cabrini, S., Calafiore, G., Lacey, I., Peroz, C., and Babin, S., "Binary pseudo-random patterned structures for modulation transfer function calibration and resolution characterization of a full-field transmission soft x-ray microscope," Rev. Sci. Instrum. 86(12), 123702/1-12 (2015); doi: 10.1063/1.4936752.
[13] Babin, S., Bouet, N., Cabrini, S., Calafiore, G., Conley, R., Gevorkyan, G., Munechika, K., Vladár, A., and Yashchuk, V. V., "1.5 nm fabrication of test patterns for characterization of metrological systems," Proc. SPIE 10145, 1014518/1-9 (2017); doi:10.1117/12.2257624.
[14] Yashchuk, V. V., Babin, S., Cabrini, S., Griesmann, U., Lacey, I., Munechika, K., Pina-Hernandez, C., and Wang, Q., "Characterization and operation optimization of large field-of-view optical interferometers using binary pseudorandom array test standard," Proc. SPIE 10749, 107490R/1-13 (2018); doi: 10.1117/12.2322011.
[15] Shapiro, D. A., Babin, S., Celestre, R., Chao, W., Conley, R. P., Denes, P., Enders, B., James, S., Joseph, J., Krishnan, H., Marchesini, S., Nowrouzi, K., Padmore, H., Warwick, T., Yang, L., Yashchuk, V. V., Yu, Y.-S., and Zhao, J., "A facility for ultra-high resolution soft x-ray microscopy and quantitative analysis of chemically heterogeneous nano-materials," Science Advances 6, eabc4904/1-8 (16 December 2020); doi: 10.1126/sciadv.abc4904.
[16] Yashchuk, V. V., Babin, S., Cabrini, S., Chao, W., Griesmann, U., Lacey, I., Marchesini, S., Munechika, K., Pina-Hernandez, C., and Roginsky, A., "Binary pseudo-random array test standard optimized for characterization of large field-of-view optical interferometers," Proc. SPIE 11490, 114900W/1-8 (2020); doi: 10.1117/12.2568309.
[17] Munechika, K., Cabrini, S., Chao, W., Lacey, I., Pina-Hernandez, C., Rochester, S., and Yashchuk, V. V., "Binary pseudo-random array test standard optimized for characterization of interferometric microscopes," Proc. SPIE 11817, 1181704/1-10 (2021); doi: https://doi.org/10.1117/12.2594995
[18] Barakat, R., "Determination of the Optical Transfer Function Directly from the Edge Spread Function," J. Opt. Soc. Am. 55, 1217-1221 (1965); doi: https://doi.org/10.1364/JOSA.55.001217.
[19] Tatian, B., "Method for Obtaining the Transfer Function from the Edge Response Function," J. Opt. Soc. Am. 55, 1014-1019 (1965); doi: https://doi.org/10.1364/JOSA.55.001014.
[20] Creath, K., "Calibration of numerical aperture effects in interferometric microscope objectives," Appl. Opt. 28 (15), 3333-3338 (1989); doi: 10.1364/AO.28.003333.
[21] Takacs, P. Z., Li, M. X., Furenlid, K., and Church, E. L., "Step-height standard for surface-profiler calibration," Proc. SPIE 1995, 235–244. (1993); https://doi.org/10.1117/12.162661.
[22] Harasaki, A. and Wyant, J.C., "Fringe modulation skewing effect in white-light vertical scanning interferometry," Appl. Opt. 39, 2101-2106 (2000); https://doi.org/10.1364/AO.39.002101.

[23] Boreman, G.D. and Yang, S., "Modulation Transfer Function Measurement Using Three- and Four-bar Targets," Appl. Opt. 34, 8050-8052 (1995); doi: 10.1364/AO.34.008050.
[24] Marchywka, M. and Socker, D. G., "Modulation transfer function measurement technique for small-pixel detectors," Appl. Opt. 31(34), 7198-7213 (1992); doi: ttps://doi.org/10.1364/AO.31.007198.
[25] Nijhawan, O. P., Datta, P. K., and Bhushan, J., "On the measurement of MTF using periodic patterns of rectangular and triangular wave-forms," Nouv. Rev. Opt. 6(1), 33-36 (1975); https://iopscience.iop.org/article/10.1088/0335-7368/6/1/304.
[26] Rhee, H. G., Vorburger, T. V., Lee, J.W., and Fu, J., "Discrepancies between roughness measurements obtained with phase-shifting and white-light interferometry," Appl. Opt. 44(28), 5919-5927 (2005); https://doi.org/10.1364/AO.44.005919.
[27] Yashchuk, V. V., Artemiev, N. A., Lacey, I., McKinney, W. R., and Padmore, H. A., "A new X-ray optics laboratory (XROL) at the ALS: Mission, arrangement, metrology capabilities, performance, and future plans," Proc. SPIE 9206, 92060I/1-19 (2014); doi:10.1117/12.2062042.
[28] Yashchuk, V. V., Artemiev, N. A., Lacey, I., McKinney, W. R., and Padmore, H. A., "Advanced environmental control as a key component in the development of ultra-high accuracy ex situ metrology for x-ray optics," Opt. Eng. 54(10), 104104 (2015); doi: 10.1117/1.OE.54.10.104104.
[29] Munechika, K., Rochester, S., Chao, W., Lacey, I., Pina-Hernandez, C., and Yashchuk, V. V., "Binary pseudo-random array standards for calibration of 3D optical surface profilers used for metrology with aspheric x-ray optics," SPIE Optics and Photonics 2022, Conference OP323: Interferometry XXI, Paper No.: OP323-16; Tracking No.: OP22O-OP323-16 (San Diego, August 21-25, 2022); this conference.
[30] Fenimore, E. E., and Cannon, T. M., "Coded aperture imaging with uniformly redundant arrays," Appl. Opt. 17(3), 337–347 (1978); doi: ttps://doi.org/10.1364/AO.17.000337.
[31] Caroli, E., Stephen, J. B., Cocco, G. Di., Natalucci, L., and Spizzichino, A., "Coded aperture imaging in x- and gamma-ray astronomy," Space Sci. Rev. 45, 349–403 (1987); doi: https://doi.org/10.1007/BF00171998.
[32] Yashchuk, V. V., Babin, S., Cabrini, S., Chao, W., Griesmann, U., Lacey, I., Marchesini, S., Munechika, K., Pina-Hernandez, C., and Roginsky, A., "Binary pseudorandom array test standard optimized for characterization of large field-of-view optical interferometers," Proc. SPIE 11490, 114900W/1-8 (2020); doi: 10.1117/12.2568309.
[33] Takacs, P. Z., Rochester, S., Lacey, I., Munechika, K., and Yashchuk, V. V., "Calibration, modeling, parameterization, and verification of the Instrument Transfer Function of an interferometric microscope," SPIE Optics and Photonics 2022, Conference OP323: Interferometry XXI, Paper No.: OP323-13; Tracking No.: OP22O-OP323-13 (San Diego, August 21-25, 2022); this conference.
[34] Rochester, S., Munechika, K., Lacey, I., Takacs, P. Z., and Yashchuk, V. V., "Super-resolution image reconstruction for surface metrology of x-ray optics," Poster presentation at the 7th International Workshop on X-ray Optics and Metrology, The SRI2022 Satellite Workshop (IWXM 2022) (Berlin, Germany, April 7, 2022).
[35] Rochester, S., English, D., Lacey, I., Munechika, K., and Yashchuk, V. V., "Super-resolution interferometric microscope measurements with x-ray variable-line-spacing diffraction gratings," SPIE Optics and Photonics 2022, Conference OP501: Advances in Metrology for X-Ray and EUV Optics X, Paper No.: OP501-5; Tracking No.: OP22O-OP501-5 (San Diego, August 21-25, 2022); this conference.
[36] Yashchuk, V. V., Lacey, I., Takacs, P. Z., and Rochester, S., "Resampling effect to instrumental transfer function calibration," (2022, in preparation).
[37] Yashchuk, V. V., Lacey, I., Arnold, T., Paetzelt, H., Rochester, S., Siewert, F., and Takacs, P.Z., "Investigation on lateral resolution of surface slope profilers," Proc. SPIE 11109, 111090M/1-19 (2019); doi: 10.1117/12.2539527.
[38] Yashchuk, V. V., Rochester, S., Lacey, I., and Babin, S., "Super-resolution surface slope metrology of x-ray mirrors," Rev. Sci. Instrum. 91, 075113/1-11 (2020); doi: 10.1063/5.0005556.
[39] Griesmann, U., Munechika, K., Chao, W., Lacey, I., Pina-Hernandez, C., Renegara, T. B., Zheng, X. A., and Yashchuk, V. V., "Binary pseudo-random arrays for instrument transfer function calibration of areal texture-measuring optical microscopes," Abstract of an oral presentation at the 23rd International Conference on Metrology and Properties of Surfaces 2022 (Met & Props 2022) (Strathclyde Glasgow, UK, June 28-30, 2022).
[40] Griesmann, U., Munechika, K., Renegara, T. B., Zheng, X. A., Soons, J. A., Chao, W., Lacey, I., Pina-Hernandez, C., Takacs, P. Z., and Yashchuk, V. V., "Characterization of surface texture-measuring optical microscopes using a binary pseudo-random array standard," SPIE Optics and Photonics 2022, Conference OP323: Interferometry XXI, Paper No.: OP323-21; Tracking No.: OP22O-OP323-21 (San Diego, August 21-25, 2022); this conference.